

Tomography of orbital vortex lines in a topological semimetal

T. Figgemeier,^{1,*} M. Ünzelmann,^{1,†} P. Eck,^{2,*} J. Schusser,¹ L. Crippa,² J. N. Neu,^{3,4} B. Geldiyev,¹ P. Kagerer,¹ J. Buck,^{5,6} M. Kalläne,^{5,6} M. Hoesch,⁷ K. Rossnagel,^{5,6,7} T. Siegrist,^{3,4} L.-K. Lim,⁸ R. Moessner,⁹ G. Sangiovanni,² D. Di Sante,¹⁰ F. Reinert,¹ and H. Bentmann^{1,11}

¹*Experimentelle Physik VII and Würzburg-Dresden Cluster of Excellence ct.qmat, Universität Würzburg, Am Hubland, D-97074 Würzburg, Germany*

²*ITPA and Würzburg-Dresden Cluster of Excellence ct.qmat, Universität Würzburg, Am Hubland, D-97074 Würzburg, Germany*

³*Department of Chemical and Biomedical Engineering, FAMU-FSU College of Engineering Tallahassee, FL 32310, USA*

⁴*National High Magnetic Field Laboratory, Tallahassee, FL 32310, USA*

⁵*Institut für Experimentelle und Angewandte Physik, Christian-Albrechts-Universität zu Kiel, D-24098 Kiel, Germany*

⁶*Ruprecht Haensel Laboratory, Kiel University and DESY, D-24098 Kiel and D-22607 Hamburg, Germany*

⁷*Deutsches Elektronen-Synchrotron DESY, D-22607 Hamburg, Germany*

⁸*Zhejiang Institute of Modern Physics, Department of Physics, Zhejiang University, Hangzhou, Zhejiang 310027, People's Republic of China*

⁹*Max Planck Institute for the Physics of Complex Systems and Würzburg-Dresden Cluster of Excellence ct.qmat, Noethnitzer Strasse 38, D-01187 Dresden, Germany*

¹⁰*Department of Physics and Astronomy, University of Bologna, I-40127 Bologna, Italy*

¹¹*Center for Quantum Spintronics, Department of Physics, NTNU Norwegian University of Science and Technology, NO-7491 Trondheim, Norway*

(Dated: February 16, 2024)

Topological defects [1] are inherently stable structures that manifest in a variety of physical settings, from particle physics [2] and cosmology [3] to superfluids [4] and quantum magnets [5]. The geometric structure of Bloch wave functions in a periodic lattice may host topological defects, underpinning the unique properties of topological quantum matter [6–20]. While pointlike defects, the celebrated Weyl points, have been extensively studied [21–23], higher dimensional structures have proven to be harder to pin down. Here, we report the experimental discovery of orbital vortex lines — the first imaging of non-trivial quantum-phase winding at line nodes — in the three-dimensional (3D) band structure of a topological semimetal, TaAs. Leveraging dichroic photoemission tomography, we directly image the winding of atomic orbital angular momentum, thereby revealing — and determining the location of — lines of vorticity in full 3D momentum space. We determine the core of the orbital angular momentum vortex to host a so-called almost movable, two-fold spin-degenerate Weyl nodal line, a topological feature predicted to occur in certain non-symmorphic crystals [24]. These results establish the capacity to detect complex topological textures in reciprocal space and may pave the way toward novel orbital transport phenomena in metallic quantum materials [25, 26].

Topological band structures have proven to be a spectacularly rich source of new phenomena in the study of quantum matter. While mathematically analogous to real space topological

defects, their physical manifestations are as distinct from that case as they are varied. Given the importance of line vortices in real space — particularly prominent in superfluids [4], superconductors [27], and indeed the early universe [3, 28] — it may seem surprising that such structures in reciprocal space have thus far entirely eluded detection. This is despite the fact that their possible existence is theoretically firmly established: pseudospin vortex rings have recently been predicted to emerge in 3D topological semimetals [4, 29], and they are likely associated with novel topological quantum transport properties [30–32].

This state of affairs is presumably in part due to the experimental challenge of imaging vorticity across extended volumes of 3D k -space, requiring a complete 3D map of the wave function properties. This we have now achieved with the necessary phase-sensitive and momentum-resolved contrast via linear and circular dichroism in soft X-ray angle-resolved photoelectron spectroscopy (SX-ARPES) [23, 33–35].

Our central result is an image of 3D reciprocal space that unambiguously exhibits topological vortex lines in the orbital texture of TaAs. This compound has attracted broad attention for hosting Weyl points [21–23, 36–38]. Recent theory has also identified it as a candidate for line nodes, on account of its non-symmorphic crystal symmetry [SG $I4_1md$ (#109)], including symmetry-enforced Weyl nodal lines (WNL) and nodal chains [24, 39]. In particular, TaAs is predicted to host so-called ‘almost movable Weyl nodal lines’ (am-WNL), which evade previous classification schemes based on com-

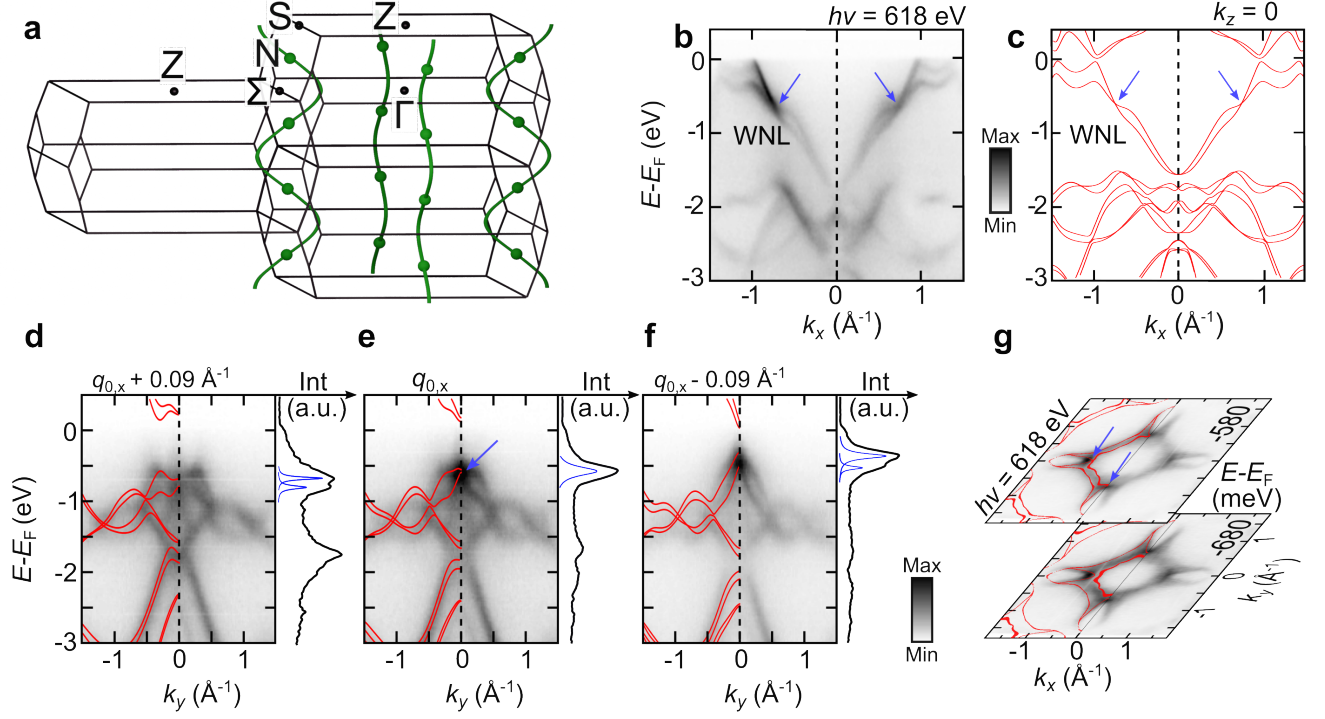


FIG. 1. **Almost movable Weyl nodal line in TaAs.** **a** Sketch of the TaAs Brillouin zone with a symmetry-enforced almost movable Weyl nodal line (WNL), denoted in green, as predicted in Ref. [24]. The WNL interconnects adjacent N points (green dots). **b, c** ARPES data and DFT calculation along the Γ - Σ direction. A band crossing corresponding to the WNL is highlighted with blue arrows. **d, e, f** ARPES data and DFT calculations along k_y taken at selected k_x near the location of the WNL. The energy distribution curves (EDC) at $k_y = 0 \text{ \AA}^{-1}$ supports a vanishing band splitting at the WNL. **g** ARPES constant-energy-cuts recorded in the Γ - Σ plane ($h\nu = 618 \text{ eV}$) at energies near the WNL (blue arrows).

patibility relations or the group structure of the involved symmetries [24]. These am-WNLs are restricted by symmetry to visit specific time-reversal-invariant momenta (TRIM) but their path through the Brillouin zone is otherwise largely unconstrained. Moreover, their protection by time-reversal and crystal symmetries implies a particular robustness of the nodal crossings.

Our work indeed establishes the nodal line we have found to be of the am-WNL type. This is backed up by detailed theoretical modeling, which provides essentially quantitative agreement with our experiments. In the following, we first analyze the band dispersion around a two-fold spin-degenerate band crossing using SX-ARPES and density functional theory (DFT) bulk band structure calculations. Subsequently, the focus will shift to the properties of the wave functions of the corresponding eigenstates. More precisely, we will investigate the 3D momentum dependence of the atomic orbital angular momentum (OAM) using dichroic SX-ARPES supported by state-of-the-art simulations of the photoemission intensity, DFT, and an effective minimal model. Finally, we utilize dichroism under systematically varied experimental parameters to achieve a full vectorial tomography of the orbital vortex texture.

In order to pin down the nodal line dispersion in TaAs, Fig-

ure 1b displays SX-ARPES data along $\Gamma\Sigma$ obtained at $h\nu = 618 \text{ eV}$, demonstrating excellent agreement with the corresponding calculation in Fig. 1c. For our analysis, we will focus on the topmost valence band which extends approximately 1.5 eV below E_F . This band exhibits a notable splitting resulting from spin-orbit coupling (SOC) and broken inversion symmetry, as confirmed by both our calculations and high-resolution data (see Supplementary Note 1 for further analysis). Interestingly, we observe a band crossing along the $\Gamma\Sigma$ path, denoted by blue arrows in Figs. 1b-c, consistent with the prediction of an am-WNL [24], outlined in Fig. 1a. Around the observed crossing at q_0 the band dispersion is highly anisotropic, and our data and calculations clearly reveal splittings along both in-plane momentum directions (Fig. 1d-g).

Tracing the band crossing along the out-of-plane momentum k_z , our DFT calculations reveal a WNL that connects neighboring N-points through the $\Gamma'ZN\Sigma$ mirror planes, confirming its classification as an am-WNL [24], as depicted in Figs. 2b,d. To experimentally verify this k_z evolution, we conducted photon-energy-dependent measurements. We obtained data sets in two energy intervals, as illustrated in Fig. 2c. Representative data sets in Fig. 2a are shown and compared to calculations at corresponding out-of-plane momenta (Fig. 2b),

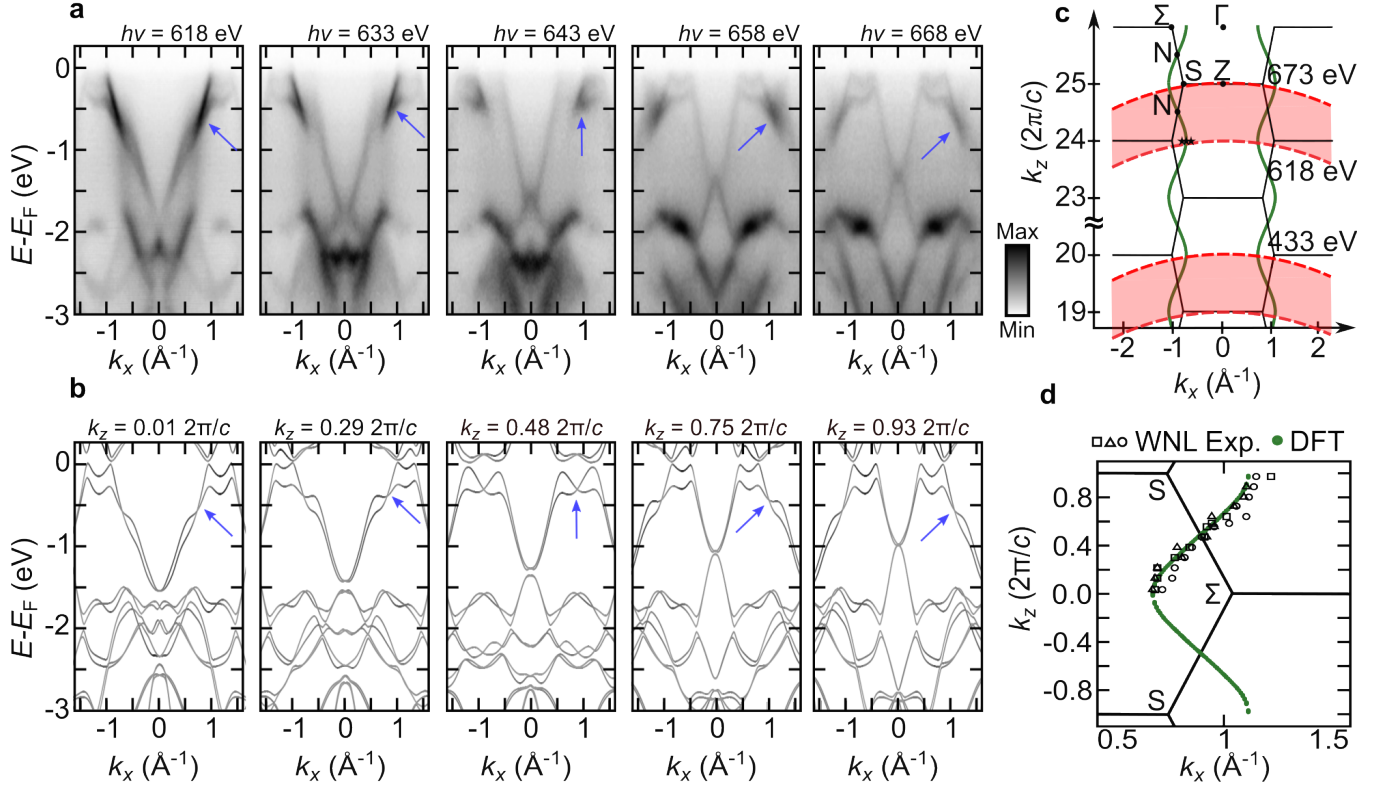


FIG. 2. **3D evolution of the Weyl nodal line.** **a** ARPES data sets along the Γ - Σ direction for various k_z throughout the Brillouin zone. Data sets are symmetrized with respect to the Γ point. **b** DFT calculations at k_z -values matching the data sets in **a**. Blue arrows mark the position of the WNL. **c** Bulk Brillouin zone structure of TaAs. Red dashed lines represent measurements at fixed photon energy $h\nu$. Data sets were taken in the red-shaded area. The stars represent the cuts shown in Figs. 1 d-f. **d** Position of the WNL based on DFT (green line) and $h\nu$ -dependent ARPES data (data points) in the upper red-shaded area of **c**.

achieving excellent agreement. Notably, a gradual shift of the band crossing towards larger k_x is observed as k_z varies from the zone center ($h\nu = 618$ eV, $k_z \approx 0$) to the ZS equi- k_z plane ($h\nu = 668$ eV, $k_z \approx 2\pi/c$). Thus, our measurements and calculations reveal a significant undulation of the WNL with k_z , where the band crossing modulates between type-II (tilted) and type-I (untilted). Importantly, we consistently observe abrupt modulations in the photoemission intensity along k_x at the band crossing for all photon energies, providing an additional spectroscopic signature of the WNL. Taken together, we plot the WNL in Fig. 2d as extracted from the experimental data (see also Supplementary Note 1) in good agreement with the overlaid calculations.

Having established the dispersion, we will now focus on the properties of the wave functions aiming to understand the orbital texture in the vicinity of the am-WNL. To this end, we calculated the orbital contributions to the Bloch states Ψ_k . Along the k_x direction, the states are predominantly formed from Ta d_{xz} and $d_{z^2} / d_{x^2-y^2}$ orbitals. Due to broken inversion symmetry, these orbitals hybridize with complex phases:

$$|\Psi_k\rangle \propto (\sqrt{3}|d_{z^2}\rangle + |d_{x^2-y^2}\rangle) + i\gamma(\mathbf{k}) \cdot |d_{xz}\rangle.$$

As a result, the states Ψ_k carry a finite atomic orbital angular

momentum (OAM) $\langle L_y \rangle \propto \gamma(k)$ and Berry curvature. Importantly, $\gamma(k)$ undergoes a sign switch at the WNL (see Supplementary Note 3), leading to a reversal of OAM and Berry curvature (Fig. 3a-b).

To address this aspect experimentally, we consider the linear dichroism (LD) in the ARPES intensity distribution (Figs. 3c,e). The LD is defined as $LD = I(k_x) - I(-k_x)$ when employing p-polarized or circularly polarized light incident in the xz plane. Similar to circular dichroism (CD) [40, 41], the LD can be associated with OAM [42]. Specifically, assuming a weak k_x dependence of the photoelectron final state, leading terms in the LD are proportional to $\gamma(k)$ (see Supplementary Note 2).

The measured LD shows good agreement with the calculated OAM and reverses sign across the WNL, confirming the predicted OAM reversal (Figs. 3c,e). To further substantiate this finding, we conducted one-step photoemission calculations (Fig. 3d,f). The results provide a striking match with the experimental data, confirming that the observed LD reversal at the WNL is a genuine effect of the photoemission matrix element. A minor exception is the appearance of a surface resonance in the calculation that is not observed in the experimental data. Comparison of LD distributions along $\Gamma\Sigma$ at different photon energies (Figs. 3c,e), which both belong to

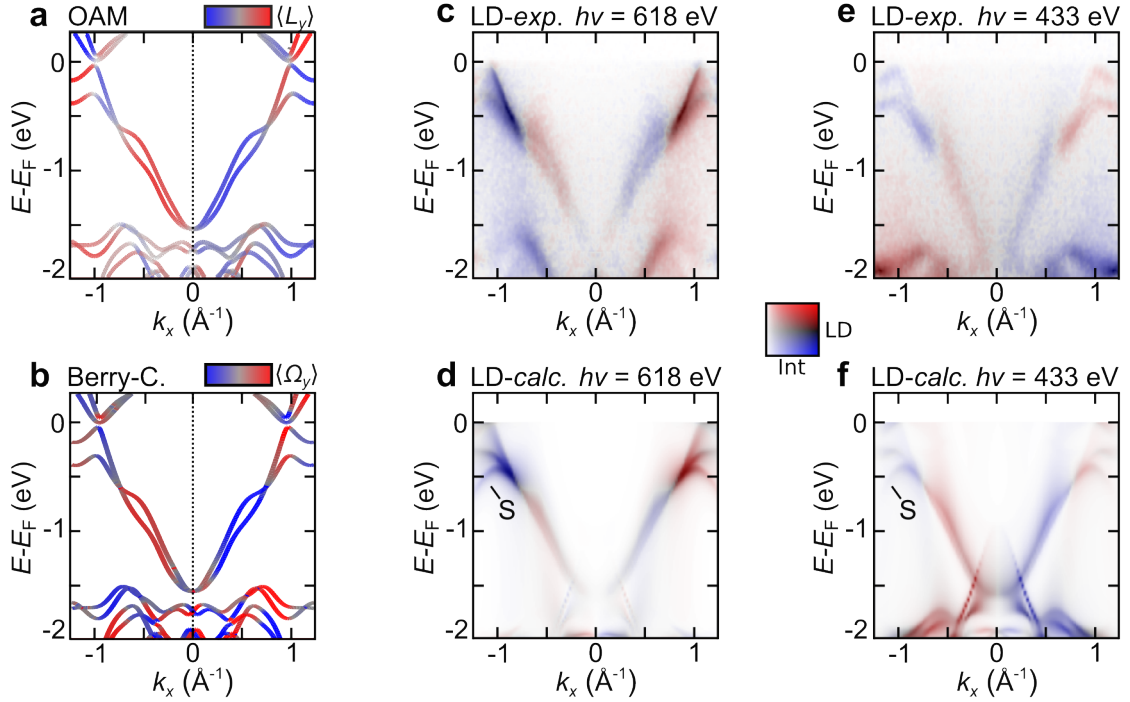


FIG. 3. **Linear dichroism, orbital angular momentum and Berry curvature at the WNL.** **a,b** OAM and Berry curvature along y obtained from DFT. Both quantities switch sign at the WNL. **c,e** Measured linear dichroism (see text) at two different photon energies, both corresponding to the same out-of-plane momentum of $k_z \approx 0$. **d,f** Same as in **c,e**, but obtained from a one-step photoemission calculation. Overall, the LD shows a sign change at the WNL crossing point in agreement to OAM and Berry curvature. A surface resonance in the calculations is marked by S .

the same k_z , indicate only a modest influence of the photoemission final state. Both the calculation and experimental data consistently display a reversal of the LD at the WNL, affirming the sensitivity of LD to the phase $\gamma(k)$ and to the OAM.

From basic symmetry considerations, it is evident that the $\Gamma Z \Sigma$ mirror planes must host symmetry-enforced lines with vanishing OAM, $L = 0$ (see Fig. 4a and Supplementary Note 3). In Fig. 4b we present the band-resolved OAM texture within the $k_x k_z$ mirror plane. Remarkably, the OAM flips sign on a curved trajectory $\mathbf{q}_0(k_z)$, where $L = 0$, that perfectly aligns with the WNL (green line). Our LD data as a function of photon energy (Fig. 4c) further validate the k_z -dependent undulation of the OAM sign reversal, consistent with the observed evolution of the WNL in Fig. 2.

To understand this crucial observation, we investigate the OAM texture in the vicinity of the WNL. For this purpose, we consider the Hamiltonian:

$$\mathcal{H}_{\text{OVL}}(\mathbf{q}) = \mathcal{H}_0 + H_{\text{ISB}}(\mathbf{q}), \quad (1)$$

where $\mathbf{q} = \mathbf{k} - \mathbf{q}_0$ (see Supplementary Note 3). \mathcal{H}_0 describes the unperturbed situation and the second account for the formation of OAM \mathbf{L} due to broken inversion symmetry. In first order, the latter can be expressed as

$$\mathcal{H}_{\text{ISB}}(\mathbf{q}) \approx -\alpha_{y,x} q_y L_x + (\alpha_{x,y} q_x - \alpha_{z,y} q_z) L_y + \alpha_{y,z} q_y L_z. \quad (2)$$

The coefficients $\alpha_{i,j}$ are real-valued parameters and quantify the energy scale associated with the breaking of inversion symmetry. The resulting OAM texture exhibits a vortex enclosing the line $\mathbf{q}_0(k_z)$. Although details depend on the k_z -dependent parameters $\alpha_{i,j}$, the OAM vortex universally carries a winding number $\nu = 1$. Our DFT calculations confirm these findings (see Fig. 4a and S7) and further show that $\alpha_{y,z}$ is small for all k_z , implying that \mathbf{L} has predominantly in-plane orientation.

There is one final ingredient missing in order to obtain the fully-fledged WNL, which is spin-orbit coupling. This lifts spin degeneracy implicit in the band structure obtained from Eq. 2. The non-trivial OAM winding texture, however, remains unaffected by the presence of SOC (see also Supplementary Note 3). In essence, the line $\mathbf{q}_0(k_z)$ serves a precursor of the WNL, around which $H_{\text{SOC}} \propto \mathbf{L} \cdot \mathbf{S}$ induces a band splitting $\Delta E \propto L$ that vanishes at \mathbf{q}_0 .

To gain experimental access to the OAM vortex, we consider the normalized circular dichroism (nCD) in k_x - k_y momentum maps. As shown recently, CD-ARPES enables detailed mapping of the in-plane momentum-space OAM texture [23, 43]. In Fig. 4d,e, we consider data sets at two photon energies, corresponding to out-of-plane momenta $k_z \approx 0$ and $k_z \approx 0.58 \, 2\pi/c$, with characteristically distinct k_{\parallel} -dispersion (compare also Fig. 2).

Within our experimental geometry, the nCD pattern is sensi-

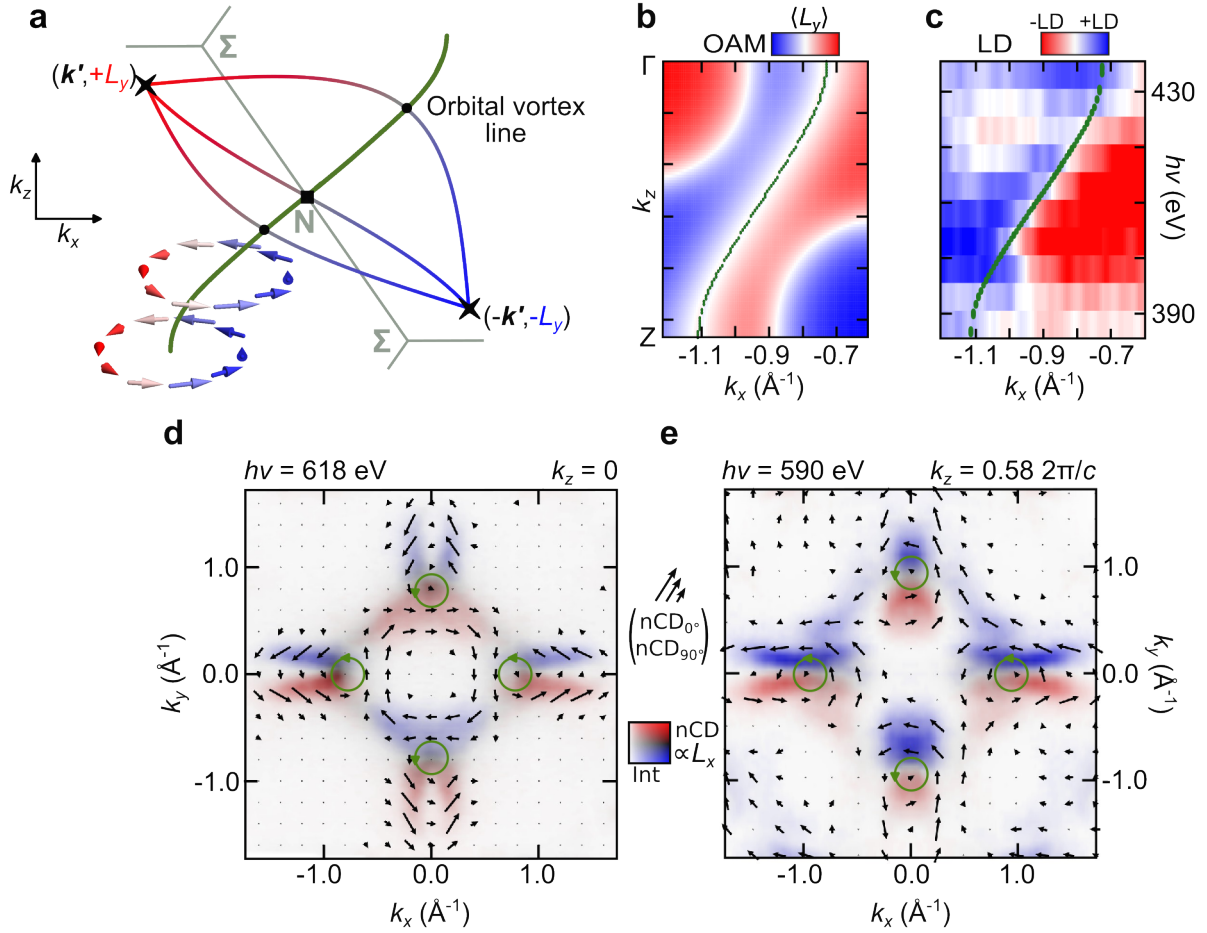


FIG. 4. Orbital vortex line in three-dimensional momentum space. **a** Illustration of symmetry-enforced formation of orbital vortex lines (OVL). DFT calculations of the OAM vortex configuration are depicted at different k_z -values. **b** DFT calculation of the OAM in the $\Gamma Z N \Sigma$ mirror plane. The green line indicates the calculated position of the WNL, matching the trajectory on which the OAM vanishes. **c** Measured LD, integrated over the energy interval of the OVL, in dependence of photon energy $h\nu$, sampling the sign change of the LD for different k_z -values throughout one BZ. **d,e** Normalized circular dichroism momentum maps obtained at photon energies $h\nu = 618$ eV and $h\nu = 590$ eV corresponding to out-of-plane momenta of $k_z \approx 0$ and $k_z \approx 0.58 \cdot 2\pi/c$, respectively. The constant energy contours are taken at the respective energy of the nodal points, i.e., -0.58 eV (**d**) and -0.38 eV (**e**). The dichroic pattern (red-blue) reflects OAM component L_x . The vectors $(nCD_{0^\circ}, nCD_{90^\circ})$ are obtained from taking the $nCD_{0^\circ}(k_x, k_y)$ and the same data set rotated by 90° . This symmetry operation ($\mathcal{R}_{90^\circ}: (k_x, k_y) \mapsto (-k_y, k_x)$) also transforms the in-plane OAM as $\mathcal{R}_{90^\circ}: L_x(k_x, k_y) \mapsto L_y(-k_y, k_x)$. The observed vector field around the nodal point momenta, highlighted by the green circles, resembles the OAM vortex winding.

tive to the in-plane OAM component L_x [23] (Supplementary Note 2). This signal — referred to as nCD_{0° — is represented by the red-blue color code in Fig. 4d,e. In addition, four-fold rotation symmetry in the crystal structure of TaAs allows us to reconstruct the full vectorial in-plane OAM texture. This means rotation of the sample by 90° transforms the in-plane OAM as $L_x(k_x, k_y) = L_y(-k_y, k_x)$. This in turn provides access to the orthogonal component $nCD_{90^\circ} \propto L_y$ and we can determine the in-plane OAM vector fields plotted as arrows in Fig. 4d,e. We directly observe vortex textures around the four nodal points (also Supplementary Fig. S7), as predicted from our model Hamiltonian (Eq. 2) and DFT calculations (Fig. 4a and Supplementary Fig. S7). This applies to both exemplary out-of-plane momenta considered,

with the positions of the vortex cores \mathbf{q}_0 varying according to the undulation of the nodal line (Figs. 2d and 4b,c).

In conclusion, our experiments provide a complete three-dimensional tomographic image of orbital vortex lines in the electronic structure of a topological quantum material. These vortices emerge as line defects in the 3D Bloch wave-function manifold, and their existence is closely tied to the band topology. Specifically, our measurement of orbital winding directly reveals a topological charge, linked to the presence of a line node. In close analogy to nodal points in surface states of topological insulators, time-reversal in conjunction with crystal symmetry underpins both orbital-momentum locking and the robust spin degeneracy in the vortex core.

The resulting almost movable Weyl nodal lines [24], observed here for the first time, thus exhibit remarkable robustness, in contrast to recently discussed magnetic Weyl loops [44, 45] that originate from accidental band crossings and are unstable to SOC [46].

Given the importance of topological band structures for technological applications ranging from quantum computation to low-dissipation electronics [6–19], the key finding of orbital vortex lines raises the prospect of exploring novel quantum transport phenomena in nodal line semimetals. In particular, our results highlight the potential of investigating these materials with regard to orbitronics [25, 47, 48]. Furthermore, the capabilities of dichroic photoemission tomography — utilized extensively in this work — may pave the way for the exploration of exotic band topologies arising from line nodes, including Nexus textures and non-Abelian topological invariants [10, 49], which have so far evaded the context of realistic quantum materials.

ACKNOWLEDGMENTS

This work is funded by the Deutsche Forschungsgemeinschaft (DFG, German Research Foundation) through SFB 1170 'ToCoTronics', the Würzburg-Dresden Cluster of Excellence on Complexity and Topology in Quantum Matter – *ct.qmat* Project-ID 390858490 - EXC 2147, and RE1469/13-2. The Research Council of Norway (RCN) supported H. B. through its Centres of Excellence funding scheme, project number 262633, “QuSpin”, and RCN project number 323766. The research leading to these results has received funding from the European Union’s Horizon 2020 research and innovation program under the Marie Skłodowska-Curie Grant Agreement No. 897276. We acknowledge DESY (Hamburg, Germany), a member of the Helmholtz Association HGF, for the provision of experimental facilities. Parts of this research were carried out at PETRA III and we would like to thank Kai Bagschik, Jens Viehhaus, Frank Scholz, Jörn Seltmann and Florian Trinter for assistance in using beamline P04. Funding for the photoemission spectroscopy instrument at beamline P04 (Contracts 05KS7FK2, 05K10FK1, 05K12FK1, 05K13FK1, 05K19FK4 with Kiel University; 05KS7WW1, 05K10WW2 and 05FK19WW2 with Würzburg University) by the Federal Ministry of Education and Research (BMBF) is gratefully acknowledged. J.S. would like to acknowledge Ján Minár for providing a computational cluster at NTC, University of West Bohemia. We gratefully acknowledge the Gauss Centre for Supercomputing e.V. (www.gauss-centre.eu) for funding this project by providing computing time on the GCS Supercomputer SuperMUC at Leibniz Supercomputing Centre (www.lrz.de). J. N. and T. S. acknowledge support from the National Research Foundation, under Grant No. NSF DMR-1606952. The crystal synthesis and characterization was carried out at the National High Magnetic Field Laboratory, which is funded by the National

Science Foundation (NSF DMR-2128556) and the State of Florida.

* These authors contributed equally to the present work.

† These authors contributed equally to the present work.; muenzelmann@physik.uni-wuerzburg.de

- [1] N. D. Mermin, *Rev. Mod. Phys.* **51**, 591 (1979), URL <https://link.aps.org/doi/10.1103/RevModPhys.51.591>.
- [2] P. A. M. Dirac, *Proc. R. Soc. London A Math. Phys. Eng. Sci.* **133**, 60 (1931).
- [3] A. Vilenkin and E. P. S. Shellard, *Cosmic strings and other topological defects* (Cambridge University Press, 1994).
- [4] G. E. Volovik, *The universe in a helium droplet*, vol. 117 (OUP Oxford, 2003).
- [5] S. Mühlbauer, B. Binz, F. Jonietz, C. Pfleiderer, A. Rosch, A. Neubauer, R. Georgii, and P. Böni, *Science* **323**, 915 (2009).
- [6] K. S. Novoselov, A. K. Geim, S. V. Morozov, D. Jiang, M. I. Katsnelson, I. V. Grigorieva, S. V. Dubonos, and A. A. Firsov, *Nature* **438**, 197 (2005).
- [7] M. Z. Hasan and C. L. Kane, *Rev. Mod. Phys.* **82**, 3045 (2010).
- [8] X.-L. Qi and S.-C. Zhang, *Rev. Mod. Phys.* **83**, 1057 (2011).
- [9] A. A. Burkov, M. D. Hook, and L. Balents, *Phys. Rev. B* **84**, 235126 (2011).
- [10] T. T. Heikkilä and G. E. Volovik, *New Journal of Physics* **17**, 093019 (2015).
- [11] C. Fang, Y. Chen, H.-Y. Kee, and L. Fu, *Phys. Rev. B* **92**, 081201 (2015).
- [12] C.-K. Chiu, J. C. Y. Teo, A. P. Schnyder, and S. Ryu, *Rev. Mod. Phys.* **88**, 035005 (2016).
- [13] B. Bradlyn, J. Cano, Z. Wang, M. Vergniory, C. Felser, R. J. Cava, and B. A. Bernevig, *Science* **353**, aaf5037 (2016).
- [14] C. Fang, H. Weng, X. Dai, and Z. Fang, *Chinese Physics B* **25**, 117106 (2016).
- [15] F. D. M. Haldane, *Rev. Mod. Phys.* **89**, 040502 (2017).
- [16] X.-G. Wen, *Rev. Mod. Phys.* **89**, 041004 (2017).
- [17] N. P. Armitage, E. J. Mele, and A. Vishwanath, *Rev. Mod. Phys.* **90**, 015001 (2018).
- [18] T. Ozawa, H. M. Price, A. Amo, N. Goldman, M. Hafezi, L. Lu, M. C. Rechtsman, D. Schuster, J. Simon, O. Zilberberg, et al., *Rev. Mod. Phys.* **91**, 015006 (2019).
- [19] J.-W. Rhim, K. Kim, and B.-J. Yang, *Nature* **584**, 59 (2020).
- [20] M. A. Wilde, M. Dödenhöft, A. Niedermayr, A. Bauer, M. M. Hirschmann, K. Alpin, A. P. Schnyder, and C. Pfleiderer, *Nature* **594**, 374 (2021).
- [21] B. Q. Lv, H. M. Weng, B. B. Fu, X. P. Wang, H. Miao, J. Ma, P. Richard, X. C. Huang, L. X. Zhao, G. F. Chen, et al., *Phys. Rev. X* **5**, 031013 (2015).
- [22] S.-Y. Xu, I. Belopolski, N. Alidoust, M. Neupane, G. Bian, C. Zhang, R. Sankar, G. Chang, Z. Yuan, C.-C. Lee, et al., *Science* **349**, 613 (2015).
- [23] M. Ünzelmann, H. Bentmann, T. Figgemeier, P. Eck, J. N. Neu, B. Geldiyev, F. Diekmann, S. Rohlf, J. Buck, M. Hoesch, et al., *Nature Communications* **12**, 3650 (2021).
- [24] M. M. Hirschmann, A. Leonhardt, B. Kilic, D. H. Fabini, and A. P. Schnyder, *Phys. Rev. Materials* **5**, 054202 (2021).
- [25] Y.-G. Choi, D. Jo, K.-H. Ko, D. Go, K.-H. Kim, H. G. Park, C. Kim, B.-C. Min, G.-M. Choi, and H.-W. Lee, *Nature* **619**, 52 (2023).

- [26] Q. Yang, J. Xiao, I. Robredo, M. G. Vergniory, B. Yan, and C. Felser, Proceedings of the National Academy of Sciences **120** (2023).
- [27] A. Abrikosov, Journal of Physics and Chemistry of Solids **2**, 199 (1957).
- [28] T. W. B. Kibble, Journal of Physics A Mathematical General **9**, 1387 (1976).
- [29] L.-K. Lim and R. Moessner, Phys. Rev. Lett. **118**, 016401 (2017).
- [30] K. Kim, J. Seo, E. Lee, K.-T. Ko, B. S. Kim, B. G. Jang, J. M. Ok, J. Lee, Y. J. Jo, W. Kang, et al., Nature Materials **17**, 794 (2018).
- [31] H. T. Hirose, T. Terashima, T. Wada, Y. Matsushita, Y. Okamoto, K. Takenaka, and S. Uji, Physical Review B **101**, 245104 (2020).
- [32] H. Kim, J. M. Ok, S. Cha, B. G. Jang, C. I. Kwon, Y. Kohama, K. Kindo, W. J. Cho, E. S. Choi, Y. J. Jo, et al., Nature Communications **13** (2022).
- [33] S. W. Jung, S. H. Ryu, W. J. Shin, Y. Sohn, M. Huh, R. J. Koch, C. Jozwiak, E. Rotenberg, A. Bostwick, and K. S. Kim, Nat. Mater. **19**, 277 (2020).
- [34] S. Beaulieu, J. Schusser, S. Dong, M. Schüler, T. Pincelli, M. Dendzik, J. Maklar, A. Neef, H. Ebert, K. Hricovini, et al., Phys. Rev. Lett. **125**, 216404 (2020).
- [35] Y. Yen, J. A. Krieger, M. Yao, I. Robredo, K. Manna, Q. Yang, E. C. McFarlane, C. Shekhar, H. Bormann, S. Stolz, et al., *Controllable orbital angular momentum monopoles in chiral topological semimetals* (2023), arXiv:2311.13217.
- [36] S.-M. Huang, S.-Y. Xu, I. Belopolski, C.-C. Lee, G. Chang, B. Wang, N. Alidoust, G. Bian, M. Neupane, C. Zhang, et al., Nat. Commun. **6**, 7373 (2015).
- [37] H. Weng, C. Fang, Z. Fang, B. A. Bernevig, and X. Dai, Phys. Rev. X **5**, 011029 (2015).
- [38] L. X. Yang, Z. K. Liu, Y. Sun, H. Peng, H. F. Yang, T. Zhang, B. Zhou, Y. Zhang, Y. F. Guo, M. Rahn, et al., Nat. Phys. **11**, 728 (2015).
- [39] T. Bzdušek, Q. Wu, A. Rüegg, M. Sigrist, and A. A. Soluyanov, Nature **538**, 75 (2016).
- [40] S. R. Park, J. Han, C. Kim, Y. Y. Koh, C. Kim, H. Lee, H. J. Choi, J. H. Han, K. D. Lee, N. J. Hur, et al., Phys. Rev. Lett. **108**, 046805 (2012).
- [41] J.-H. Park, C. H. Kim, J.-W. Rhim, and J. H. Han, Phys. Rev. B **85**, 195401 (2012).
- [42] M. Ünzelmann, H. Bentmann, P. Eck, T. Kißlinger, B. Geldiyev, J. Rieger, S. Moser, R. C. Vidal, K. Kißner, L. Hammer, et al., Phys. Rev. Lett. **124**, 176401 (2020).
- [43] J. Schusser, H. Bentmann, M. Ünzelmann, T. Figgemeier, C.-H. Min, S. Moser, J. N. Neu, T. Siegrist, and F. Reinert, Phys. Rev. Lett. **129**, 246404 (2022).
- [44] I. Belopolski, K. Manna, D. S. Sanchez, G. Chang, B. Ernst, J. Yin, S. S. Zhang, T. Cochran, N. Shumiya, H. Zheng, et al., Science **365**, 1278 (2019).
- [45] I. Belopolski, G. Chang, T. A. Cochran, Z.-J. Cheng, X. P. Yang, C. Hugelmeier, K. Manna, J.-X. Yin, G. Cheng, D. Multer, et al., Nature **604**, 647 (2022).
- [46] D. Liu, E. Liu, Q. Xu, J. Shen, Y. Li, D. Pei, A. Liang, P. Dudin, T. Kim, C. Cacho, et al., npj Quantum Materials **7**, 11 (2022).
- [47] B. A. Bernevig, T. L. Hughes, and S.-C. Zhang, Physical Review Letters **95** (2005).
- [48] D. Go, D. Jo, H.-W. Lee, M. Kläui, and Y. Mokrousov, EPL (Europhysics Letters) **135**, 37001 (2021).
- [49] Q. Wu, A. A. Soluyanov, and T. Bzdušek, Science **365**, 1273 (2019).
- [50] G. Kresse and J. Furthmüller, Phys. Rev. B **54**, 11169 (1996).
- [51] G. Kresse and D. Joubert, Phys. Rev. B **59**, 1758 (1999).
- [52] P. E. Blöchl, Phys. Rev. B **50**, 17953 (1994).
- [53] J. P. Perdew, K. Burke, and M. Ernzerhof, Phys. Rev. Lett. **77**, 3865 (1996).
- [54] S. Steiner, S. Khmelevskyi, M. Marsmann, and G. Kresse, Phys. Rev. B **93**, 224425 (2016).
- [55] A. A. Mostofi, J. R. Yates, Y.-S. Lee, I. Souza, D. Vanderbilt, and N. Marzari, Comput. Phys. Commun. **178**, 685 (2008).

METHODS

Experimental details

Soft X-ray angle-resolved photoemission spectroscopy (SX-ARPES) experiments were carried out at the ASPHERE III endstation at the Variable Polarization XUV Beamline P04 of the PETRA III storage ring at DESY (Hamburg, Germany). ARPES data were conducted at sample temperatures of approximately 50 K and the energy resolution of the ARPES measurements was set to $\Delta E \approx 60$ meV for the high-resolution measurements (Fig. 1b, 2a, 3) and $\Delta E \approx 90$ meV if full momentum maps have been taken (Fig. 1d-g, 4). We used the deflection mode of the SCIENTA DA30-L analyzer allowing for data acquisition in a fixed sample geometry. The angle of light-incidence in the setup is $\alpha \approx 20^\circ$. TaAs single crystals were cleaved *in situ* with a top-post at a temperature below 100 K and a pressure better than $5 \cdot 10^{-9}$ mbar. Details on chemical vapor transport growth of TaAs single crystals can be found in Ref. [23].

Theoretical details We consider in our theoretical study the non-centrosymmetric primitive unit cell of TaAs (space group $I4_1md$) with a lattice constant of 6.355 Å. We employ state-of-the-art first-principles calculations based on density functional theory as implemented in the Vienna ab-initio simulation package (VASP) [50], within the projector-augmented-plane-wave (PAW) method [51, 52]. The generalized gradient approximation as parametrized by the PBE-GGA functional for the exchange-correlation potential is used [53] by expanding the Kohn-Sham wave functions into plane-waves up to an energy cut-off of 400 eV. We sample the Brillouin zone on an $8 \times 8 \times 8$ regular mesh by including spin-orbit coupling (SOC) self-consistently [54]. For the calculation of the OAM, the Kohn-Sham wave functions were projected onto a Ta *s*, *p*, *d*- and As *s*, *p*-type tesseral harmonics basis as implemented in the WANNIER90 suite [55]. The OAM expectation values were then obtained in the atomic centred approximation by rotating the tesseral harmonics basis into the eigenbasis of the OAM operator, i.e. the spherical harmonics.

The one-step model photoemission calculations were performed within the Spin-Polarized-Relativistic Korringa-Kohn-Rostoker (SPR-KKR) package based on Green's function formalism. We used the same structural input and exchange-correlation potential as in Ref. [43]. The calculations give access to a photoemission signal with an accurate angular dependence of ARPES spectral weight by taking into

account experimental geometry, energy, and polarization of photons as well as multiply-scattered final state with a given surface termination.

MÜ and HB wrote the manuscript with contributions from PE, LC, JS, GS, DdS, LKL, RM, and FR. MÜ and HB conceived and planned the project.

AUTHORS CONTRIBUTIONS

TF and MÜ performed the experiments, with support from HB, BG, PK, JB, MH, MK, and KR. TF and MÜ analyzed the experimental data supported by PK. PE performed the first-principles calculations. JS performed the one-step photoemission calculations. JNN, TF and TS synthesized and characterized the TaAs samples. MÜ and LKL developed the model Hamiltonian with support from TF and PK. All authors contributed to the interpretation and discussion of the results. TF,

DATA AVAILABILITY STATEMENT

The data that support the findings of this study are available from the corresponding author upon reasonable request.

COMPETING FINANCIAL INTERESTS

The authors declare no competing financial interests.